Received 25 September 2023
Revised 8 December 2023
Accepted 11 December 2023

Numerical modelling and experimental validation of dripping, jetting and whipping modes of gas dynamic virtual nozzle

Krištof Kovačič and Jurij Gregorc
Laboratory for Fluid Dynamics and Thermodynamics, Faculty of Mechanical Engineering, University of Ljubljana, Ljubljana, Slovenia, and

Božidar Šarler
Laboratory for Fluid Dynamics and Thermodynamics, Faculty of Mechanical Engineering, University of Ljubljana, Ljubljana, Slovenia, and Laboratory for Simulation of Materials and Processes, Institute of Metals and Technology, Ljubljana, Slovenia

Abstract

Purpose – This study aims to develop an experimentally validated three-dimensional numerical model for predicting different flow patterns produced with a gas dynamic virtual nozzle (GDVN).

Design/methodology/approach – The physical model is posed in the mixture formulation and copes with the unsteady, incompressible, isothermal, Newtonian, low turbulent two-phase flow. The computational fluid dynamics numerical solution is based on the half-space finite volume discretisation. The geo-reconstruct volume-of-fluid scheme tracks the interphase boundary between the gas and the liquid. To ensure numerical stability in the transition regime and adequately account for turbulent behaviour, the k-ω shear stress transport turbulence model is used. The model is validated by comparison with the experimental measurements on a vertical, downward-positioned GDVN configuration. Three different combinations of air and water volumetric flow rates have been solved numerically in the range of Reynolds numbers for airflow 1,009–2,596 and water 61–133, respectively, at Weber numbers 1.2–6.2.

Findings – The half-space symmetry allows the numerical reconstruction of the dripping, jetting and indication of the whipping mode. The kinetic energy transfer from the gas to the liquid is analysed, and

The authors wish to thank Dr Saša Bajt and Prof Henry Chapman from DESY (Hamburg, Germany), a member of the Helmholtz Association HGF, for their support and valuable comments regarding the manuscript. The authors would also like to thank Dr Rizwan Zahoor (LFDT)for practical advices regarding the numerical simulation.

Funding: Funding for this research is provided by the Centre for Free-Electron Laser Science (CFEL) under the project: Innovative methods for imaging with the use of x-ray free-electron laser(XFEL) and synchrotron sources: simulation of gas-focused micro-jets, and Slovenian Grant and Innovation Agency (ARIS) within core funding P2-0162, project J2-4477 and Young Researcher Program.

Disclosure statement: No potential conflict of interest was reported by the authors.

International Journal of Numerical Methods for Heat & Fluid Flow
Vol. 34 No. 4, 2024
pp. 1582-1608
Emerald Publishing Limited
0961-5539
DOI 10.1108/HFF-09-2023-0573

locations with locally increased gas kinetic energy are observed. The calculated jet shapes reasonably well match the experimentally obtained high-speed camera videos.

Practical implications – The model is used for the virtual studies of new GDVN nozzle designs and optimisation of their operation.

Originality/value – To the best of the authors' knowledge, the developed model numerically reconstructs all three GDVN flow regimes for the first time.

Keywords Flow-focusing, Dripping, Jetting, Whipping, Gas dynamic virtual nozzle, CFD

Paper type Research paper

1. Introduction

Knowledge and understanding of fluids-related phenomena were always vital for humankind. In recent decades, interest in scientific investigations and technological applications of fluids has turned from macro to micro-scale, i.e. microfluidics (Nguyen *et al.*, 2019). Knowledge of microfluidics is a basis for precise manipulation of fluids on a submillimetre level. It enables the production of different micro-fluid entities, such as jets, drops, bubbles, capsules, emulsions and sprays (Gañán-Calvo *et al.*, 2013).

One of the possible production techniques is flow focusing (FF), where an external co-flowing fluid is applied around the internal flow (Gañán-Calvo *et al.*, 2013). This technique was first introduced by Gañán-Calvo (1998). In the most common FF method, the pressure gradient induced by an outer gas focuses liquid meniscus, which emits a jet from its tip and breaks up into droplets further downstream (Gañán-Calvo *et al.*, 2013). However, FF could also be used in liquid–liquid configuration (Anna *et al.*, 2003).

FF technique is used in many fields such as biotechnology, cytology, drug or sample delivery, pharmacy, chemistry, industrial engineering and the food and agriculture industry (Gañán-Calvo *et al.*, 2013) to mention a few.

The FF technology relies on suitable geometrical configuration and proper process parameters. Two of the most common designs used today are micro-channel and micro-nozzle configurations. FF based on a micro cross-channel principle has been mainly used to produce droplets (Chen *et al.*, 2021; Huang and Yao, 2022; Jafari and Shamloo, 2023; Khater *et al.*, 2021; Pan *et al.*, 2020; Zeng and Fu, 2020), capsules (Aghaei *et al.*, 2021) and emulsions (Ontiveros *et al.*, 2020) and for the bio-fabrication of hydrogel fibres (Guimarães *et al.*, 2021) and cell-laden hydrogel microspheres (Nguyen and Seo, 2022).

FF on the micron level was used to produce fibres of polyvinylpyrrolidone down to the nanometre thickness (Ponce-Torres *et al.*, 2019) and for smooth printing of viscoelastic microfilms (Ponce-Torres *et al.*, 2017). Dripping and jetting of microfluidic multiphase flow were applied to particle and fibre synthesis (Nunes *et al.*, 2013). The dripping regime is widely used in biotechnology to produce droplets (Dewandre *et al.*, 2020; Duan *et al.*, 2016; Segers *et al.*, 2016), multilayered droplets (Si *et al.*, 2015), microcapsules (Mu *et al.*, 2020; Si *et al.*, 2016) and emulsions (Evangelio *et al.*, 2016; Wu *et al.*, 2018; Yu *et al.*, 2019, 2021).

The most common FF micro nozzle geometric configuration is gas dynamic virtual nozzle (GDVN). It was developed by DePonte *et al.* (2008) and manufactured by flame polishing, later fabricated with ceramic moulding (Beyerlein *et al.*, 2015) and finally with three-dimensional (3D) printing (Knoška *et al.*, 2020; Nelson *et al.*, 2016). GDVNs can produce various types of FF regimes (Si *et al.*, 2009), including:

- dripping – periodic ejection of droplets formed at the nozzle outlet;
- jetting – a continuous and stable fluid entity which breaks into a stream of droplets;

- whipping – a continuous and unstable fluid entity with lateral movement perpendicular to the jet axis; and
- spurting – unstable and non-continuous fluid entity, which is interrupted periodically or randomly without knowing a period of continuous jet or droplets ejection from the nozzle.

Because of the variety of operating modes, GDVNs have been positioned in many applications. One of the most common ones is sample delivery in Serial Femtosecond Crystallography (SFX) (Chapman *et al.*, 2011) and in ultrafast laser-driven sources based on high-order harmonic generation (Klimešová *et al.*, 2021), where the jetting regime is used. However, GDVNs were also applied to produce droplets, whose size is a few 100 nanometres (Mühlig *et al.*, 2019). The jetting and the whipping regimes were combined to fabricate uniform polymer and composite micro- and nano-fibres (Vasireddi *et al.*, 2019).

Numerical simulations can be used to optimise geometric configurations of GDVNs and thus reduce production and testing costs compared to experiments (Trebbin *et al.*, 2014). Many computational fluid dynamics (CFD) approaches to investigate FF jet behaviour have been analysed recently. Most rely on the axisymmetric description, which has the benefit of a smaller computational domain in terms of cell number and, therefore, a shorter computational time than the whole 3D simulation. The drawback of the axisymmetric numerical simulation is reflected in an inability to treat the entire fluid domain appropriately. Some parts of the FF devices cannot be described as axisymmetrical, e.g. elbows, structural components and turns in the supplying part of the geometry. Therefore, most studies investigate only the nozzle tip part of these devices and assume uniform radial velocity distribution (Chen *et al.*, 2015; Mu *et al.*, 2018a, 2019, 2018b; Rahimi *et al.*, 2019, 2020; Šarler *et al.*, 2021; Wu *et al.*, 2017; Yu *et al.*, 2021; Zahoor *et al.*, 2018a, 2018b, 2019, 2020, 2021; Zhao *et al.*, 2020, 2019a, 2019b), fully developed, radially parabolic flow (Hua *et al.*, 2007; Soroor *et al.*, 2021) or a combination of both (Acero *et al.*, 2012; Blanco-Trejo *et al.*, 2020; Cabezas *et al.*, 2021; Cruz-Mazo *et al.*, 2017; Dewandre *et al.*, 2020; Herrada *et al.*, 2008; Jensen *et al.*, 2006; Mamet *et al.*, 2017; Rubio *et al.*, 2021; Vega *et al.*, 2010, 2014). Another problem of the two-dimensional axisymmetric approach is manifested in the inability to appropriately deal with the whipping regime (Blanco-Trejo *et al.*, 2020). Therefore, it is impossible to analyse all three most common FF flow regimes, which are dripping, jetting and whipping, in axisymmetry. Some researchers successfully implemented jetting and dripping flow regimes into their numerical simulations at the same nozzle geometry design (Chen *et al.*, 2015; Dewandre *et al.*, 2020; Hua *et al.*, 2007; Wu *et al.*, 2017). On the other hand, Zhao *et al.* (2019a) investigated jetting and turbulent flow regime, which is similar to whipping, with a difference in chaotic lateral movement from the axis. In contrast, in the whipping flow regime, the lateral movement of the jet around the axis could be described deterministically.

A 3D description has to be used to overcome the shortcomings of the axisymmetric approach. So far, the 3D numerical simulations of FF devices are extremely rare. Han *et al.* (2019) analysed squeezing, dripping and jetting regimes in a cross-channel configuration. Khater *et al.* (2020) implemented a 3D numerical simulation for lab-on-chip technology, where the dripping type of operating mode is a primary focus of the research. Again, a cross-channel geometry with uniform velocity inlet boundary condition was investigated.

In addition to cross-channel, also a few 3D numerical simulations of FF nozzles were investigated. In the first one, Müller *et al.* (2016) analysed a simplified domain of the 3D injector system, where the primary jet breakup was investigated using large eddy simulation (LES) for highly turbulent flow, which is used in the biogas technology field. In the second one, Belšak *et al.* (2021) investigated a gas-focused liquid micro-sheet. The third example contains a rectangular nozzle, where the rounded jets in the dripping and jetting regime were simulated by Inguva *et al.* (2019). The last example is a recent study of GDVN,

where Nazari *et al.* (2023) compared simulated jet lengths with experimental measurements. Until now, only the simplified geometry of the nozzle tip was considered, omitting geometrically complex supplying part of the nozzle that dictates velocity distribution at the nozzle tip. The nozzle inlet boundary conditions were implemented as velocity profiles, calculated from the flow rates (Müller *et al.*, 2016; Nazari *et al.*, 2023) or with the inlet tubes long enough for a fully developed flow (Belšak *et al.*, 2021; Inguva *et al.*, 2019). However, the supplying part of the nozzle can cause non-parabolic or non-uniform flow conditions far from being able to be coped axisymmetrically.

The purpose of this paper is the analysis of all three most common (dripping, jetting and whipping) GDVN operating modes (patterns), depending on the air and water flow rates at the same nozzle geometric design, however ten times larger than typically used in DESY for femtosecond crystallography (Knoška *et al.*, 2020). Ten times scale-up was used due to the limits of nozzle fabrication and accessible experimental manipulations. The model also copes with the upper or supplying part of the nozzle, which distributes air to the air–water mixing zone between the nozzle orifice and feeding capillary. The geometry design with the elbow influences the airflow conditions. Therefore, we cannot assume that air has a uniform (constant) velocity profile, as it is usually defined in numerical simulations at the air inlet boundary conditions. Numerical results are compared with our experimental data. One of the present paper's goals is to find out if the half-space 3D model is adequate for simulating all the experimentally observed GDVN phenomena. The main limitation of the half-space 3D model is the inability to deal with corkscrew whipping mode. However, to detect a whipping, the proposed model is found to be appropriate.

2. Physical model and numerical solution

2.1 Governing equations

Analysis of incompressible, unsteady, isothermal, Newtonian, two-phase, turbulent flow is carried out within ANSYS Fluent simulation system, which is based on the finite volume method (FVM). The volume in which the jet is emanating is at atmospheric pressure. Thus, we can assume that there is no significant expansion of the air and respective change in its density, so we assumed incompressible flow and neglected the energy conservation equation. Owing to the high velocities of a liquid micro-jet and micro-dimensionality of a nozzle system, one can estimate that acceleration is some hundred (or even thousand) times higher than the gravitational one. Thus, the gravitational force term in the momentum equation could be neglected. The governing equations used in our model are mass (1), momentum (2) and phase fraction (6) conservation equations:

$$\frac{\partial \rho}{\partial t} + \nabla \cdot (\rho \boldsymbol{v}) \ = 0 \tag{1}$$

$$\frac{\partial}{\partial t}(\rho \boldsymbol{v}) + \nabla \cdot (\rho \boldsymbol{v}\boldsymbol{v}) = -\nabla p + \nabla \cdot \overline{\boldsymbol{\tau}} + \boldsymbol{f}_{\sigma} \tag{2}$$

Where ρ denotes mixture density, $\boldsymbol{v}(\boldsymbol{p}, t)$ velocity, $p(\boldsymbol{p}, t)$, pressure and $\overline{\boldsymbol{\tau}}$ the Newtonian viscous stress tensor, defined as $\overline{\boldsymbol{\tau}} = \mu_{eff}(\nabla \mathbf{v} + \nabla \mathbf{v}^{\mathbf{T}})$. μ_{eff} stands for the effective dynamic viscosity of the mixture that might also include the turbulent correction and $\boldsymbol{f}_{\sigma}(\boldsymbol{p}, t)$ for the surface tension force, calculated as:

$$\boldsymbol{f}_{\sigma} = \sigma \kappa \boldsymbol{n} \tag{3}$$

where σ is surface tension, $\boldsymbol{n} = \nabla \alpha$ is normal on the gas-liquid interphase boundary, pointing from the gas to the liquid, and κ is a curvature of the interphase boundary, calculated based on the continuum surface model (CSF) as:

$$\kappa(\alpha) = -\nabla \cdot (\nabla\alpha/|\nabla\alpha|) \tag{4}$$

The volume-of-fluid (VOF) interphase boundary treatment introduces a phase indication variable $\alpha(\boldsymbol{p}, t)$, which takes values between 0 and 1, as follows:

$$\alpha(\boldsymbol{p}, t) = \begin{cases} 1 & \boldsymbol{p} \text{ in liquid} \\ 0 & \boldsymbol{p} \text{ in gas} \end{cases} \tag{5}$$

The gas–liquid interphase boundary is described by an advection equation with a discontinuity in α at the interphase boundary:

$$\frac{\partial}{\partial t}(\rho\alpha) + \nabla \cdot (\rho \boldsymbol{v}\alpha) \ = 0 \tag{6}$$

The material properties, such as dynamic viscosity and density, are determined by the phase-weighted average:

$$\vartheta(\alpha) = \alpha\vartheta_1 + (1 - \ \alpha)\vartheta_g \tag{7}$$

where ϑ_1 and ϑ_g stand for liquid and gas properties, respectively.

Because the predicted air Reynolds number in the nozzle's orifice area falls for the experimental conditions observed in the transition regime between turbulent and laminar flow, we use the k-ω shear stress transport (SST) model with two additional transport equations for k and ω, as follows:

$$\frac{\partial}{\partial t}(\rho k) + \nabla \cdot (\rho k \boldsymbol{v}) = \nabla \cdot \left(\left(\mu + \frac{\mu_t}{\sigma_k} \right) \nabla k \right) + G_k - Y_k + S_k + G_b \tag{8}$$

$$\frac{\partial}{\partial t}(\rho\omega) + \nabla \cdot (\rho\omega \boldsymbol{v}) = \nabla \cdot \left(\left(\mu + \frac{\mu_t}{\sigma_\omega} \right) \nabla\omega \right) + G_\omega - Y_\omega + S_\omega + G_{\omega b} \tag{9}$$

In these equations, G_k represents the generation of turbulence kinetic energy due to mean velocity gradients. G_ω represents the generation of ω. Y_k and Y_ω represent the dissipation of k and ω due to turbulence. S_k and S_ω are user-defined source terms. G_b and $G_{\omega b}$ account for buoyancy terms. Detailed information on the k-ω SST model, its numerical implementation and its use are provided in Fluent (2020). The effective viscosity is calculated as

$\mu_{eff} = \alpha\mu_1 + (1 - \alpha)\mu_g + \mu_t$. For the micro geometry used at DESY for SFX, the regime is laminar and the $k - \omega$ equations do not need to be used and $\mu_t = 0$ Pas.

2.2 Discretisation schemes

The described system of equations is solved on the high-performance computing (HPC) cluster (Intel Xeon E5-2680V3 processors, 2.5 GHz), with ANSYS Fluent solver, release 20.1. The SIMPLEC scheme is used for the pressure–velocity coupling, and the gradient is least square cell-based. Discrete values of pressure are calculated with PRESTO! scheme. For the momentum, k and ω equation the second order upwind is used. Two-phase flow is modelled with VOF model, where the air is set as primary (continuous) and water as secondary (dispersed) phase. VOF is solved during every iteration with a geo-reconstruct scheme to track the interface. Transient formulation of the VOF equation is calculated with an explicit

scheme. All other governing equations are calculated with the first-order implicit scheme with adaptive timestep. The limiting global Courant number is set to 0.5, and the local Courant number associated with the phase transport equation to 0.25. The absolute convergence criteria of residuals within one timestep is set to 1E-4 for continuity and 1E-5 for all velocity components, k and ω. The maximum number of iterations per one-time step is set to 30. This is enough to guarantee the residuals' convergence.

2.3 Geometric three dimensional model and spatial discretisation

A half section of the 3D printed nozzle is shown in Figure 1(a). The fluid domain is extracted from CAD model of FF nozzle with characteristic dimensions shown in Figure 1(b). As the nozzle geometry is symmetric in one direction, a half-space symmetry is imposed to extensively economise the simulations. Beyond the nozzle outlet, an external field area is designed, as shown in Figure 2(a), with a diameter of 6 mm (10×D) and a length of 25 mm, to reduce the influence of the finite discretisation volume and related boundary conditions.

The FVM meshing is set in ANSYS Meshing. It results in an unstructured, fully conformal mesh, consisting of hexahedral and tetrahedral elements, shown in Figure 2(b). In the area of higher interest, especially where the interaction between the liquid and gas occurs (e.g. area between the nozzle capillary and orifice and in the region after the nozzle outlet), the mesh consists of refined structured hexahedral elements [seen in Figure 2(d)]. Further from that focus area, the mesh element size increases, minding the cells' growth factor and equal cell size between the different mesh regions. As the complex wall geometry in the air-supplying part of the nozzle directly influences the air velocity field and not the interface reconstruction, the unstructured mesh with tetrahedral elements is prescribed.

2.4 Material properties

The material properties for both fluids at the ambient conditions used in the numerical simulation are given in Table 1, with the analysed gas (air) and liquid (water) volumetric flow rates. From now on, the abbreviation GxLy stands for "G" – gas, "x" – volumetric flow rate of gas (air) measured in [L h^{-1}], "L" – liquid and "y" – volumetric flow rate of liquid (water) measured in [μL min^{-1}] of liquid (water), e. g. G2L5 stands for a gas flow rate of 2 L h^{-1} and a water flow rate of 5 μL min^{-1}. Three cases with different air and water flow rate combinations have been simulated. The ranges of their dimensionless numbers are given in Table 2.

Reynolds number for gas is calculated at the nozzle orifice and minding the area occupied by

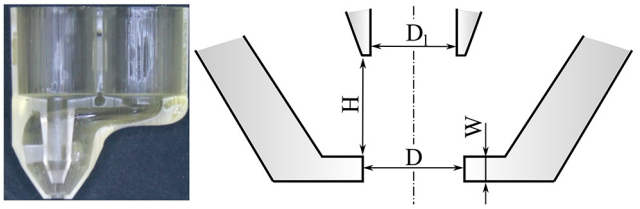

Notes: (a) Half-section of a 3D printed nozzle; (b) schematic representation of nozzle tip: capillary diameter Dl = 0.5 mm, orifice diameter D = 0.6 mm, capillary-to-orifice distance H = 0.6 mm, orifice thickness W = 0.15 mm

Source: Figure by authors

Figure 1. Representation of nozzle design

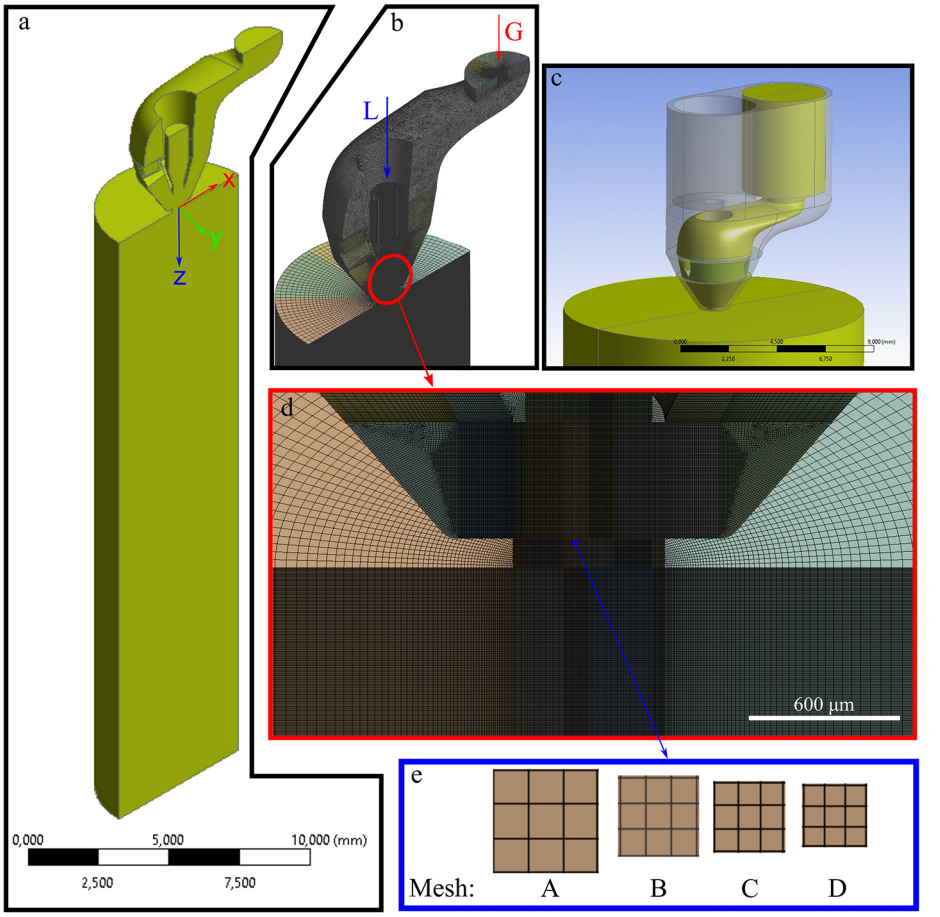

Figure 2.
Computational mesh of three-dimensional FF nozzle

Notes: (a) Half-section of the fluid domain; (b) mesh detail part of FF nozzle: (G) gas inlet; (L) liquid inlet; (c) extracted fluid domain from nozzle geometry; (d) mesh detail of mixing area inside the nozzle; (e) different types of mesh from coarser to the finest (A–D). Detailed mesh properties are shown in Table 3
Source: Figure by authors

the liquid jet as follows:

$$\mathrm{Re}_g = \frac{4\ \rho_g Q_g}{\pi \mu_g\ (D - D_j)} \tag{10}$$

Liquid Reynolds number and Weber number are defined as follows (Herrada *et al.*, 2008):

$$\mathrm{Re}_l = \frac{2}{\mu_l} \left(\frac{\rho_l^3\ \Delta p_g}{8\ \pi^2} \right)^{1/4} Q_l^{1/2} \tag{11}$$

$$\mathrm{We} = \frac{1}{\sigma}\left(\frac{8\ \rho_l \Delta p_g^3}{\pi^2}\right)^{1/4} Q_l^{1/2} \tag{12}$$

where ρ_l and ρ_g denotes the density of a liquid and gas phase, respectively, Δp_g pressure drop of a gas phase, Q_l and Q_g the volumetric flow rate of a liquid and gas phase, μ_l and μ_g dynamic viscosity of a liquid and gas, respectively, D orifice diameter and D_j liquid jet diameter. Capillary number Ca is defined as a ratio between Weber number We and Reynolds number of the liquid $\mathrm{Re_l}$. In Table 2, non-dimensional numbers are calculated based on numerical results (Δp_g and D_j) and material properties from Table 1. The non-dimensional numbers of a typical SFX nozzle operation have been added to the Table 2, according to Zahoor *et al.* (2018b). As only the jetting is used in SFX, the comparison is limited to the non-dimensional numbers of the jetting. As one can see from the Table 2, the results from the ten times scale-up nozzle partially overlap with the actual size of GDVN.

2.5 *Boundary, initial and operating conditions*

The domain comprises five boundary patches: air and water inlet, outlet, walls and symmetry. The boundary conditions at the nozzle half-space are of the symmetrical type. The solid walls are described with no-slip boundary conditions. The inlet boundary conditions for air and water are set as velocity inlets, with uniform velocity, calculated from the volumetric flow rates and a cross-sectional area at the inlet location. The pressure outlet boundary condition around the external field chamber is set to atmospheric pressure, where the gauge pressure equals zero. All prescribed boundary conditions are shown in Figure 3.

The 3D two-phase flow transient simulation is initialised with a steady–state air velocity field of the desired air flow rate, calculated separately. For the two-phase simulations, the entire inner capillary tube is initialised (at $t = 0$ s) and patched with the water, whereas the

Physical parameter	Symbol	Unit	Value/range
Air density	ρ_g	kg m^{-3}	1.225
Air viscosity	μ_g	Pa s	1.7894×10^{-5}
Water density	ρ_l	kg m^{-3}	998.2
Water viscosity	μ_l	Pa s	1.003×10^{-3}
Surface tension	σ	N m^{-1}	0.072
Air flow rate	Q_g	L h^{-1}	25, 40, 60
Water flow rate	Q_l	μL min^{-1}	500, 1000

Source: Table by authors

Table 1. Physical properties

Case	Q_g [L h^{-1}]	Q_l [μL min^{-1}]	$\Delta\rho_g$ [mbar]	$\mathrm{Re_g}$	$\mathrm{Re_l}$	We	Ca
G25L500	25	500	9.8	1009	61	1.2	0.020
G40L1000	40	1000	25.7	1842	109	3.5	0.032
G60L1000	60	1000	55.7	2596	133	6.2	0.047
SFX jetting*	–	–	–	17–1223	110–215	2.8–320	0.025–1.49

Note: *Zahoor *et al.* (2018b)

Table 2. Cases and dimensionless numbers of ten times scale-up model and actual GDVN used in SFX

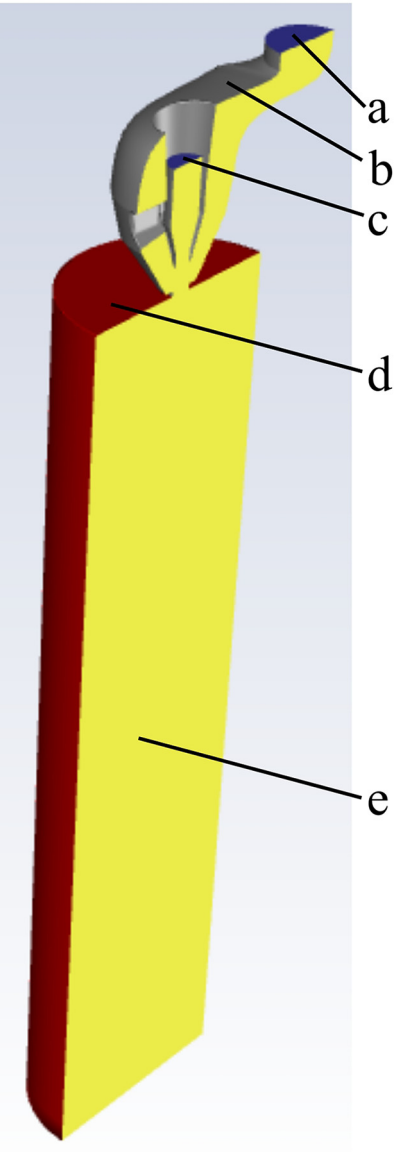

Notes: (a) Air velocity inlet (blue); (b) no-slip wall (grey); (c) water velocity inlet (blue); (d) pressure outlet (red); (e) symmetry (yellow)
Source: Figure by authors

Figure 3.
Boundary conditions

rest of the fluid domain is with the air. In such a way, the calculation time needed for the developed air flow field in a two-phase transient simulation is reduced significantly.

Simulation data is saved at 2 μs intervals, which is enough to track droplets that break up from the jet. Results are analysed using ANSYS CFD Post, Python with cv2 and Matplotlib library.

2.6 Mesh independence study

Four different meshes (A–D) are produced to assess the mesh independence. Their minimum cell sizes are shown in Table 3. After the equal reduction of cell size in all three dimensions, the mesh refinement factors, relatively scaled to mesh D, are 0.25, 0.54, 0.74 and 1.0, resulting in a total of 2,736,084, 5,916,786, 8,224,138 and 11,055,127 cells from the coarse to the finest mesh (A–D), respectively.

For the mesh independence study, calculations at conditions G40L1000 are made. The calculations are initialised based on results from mesh D at a flow time equal to 3.746 ms for all the meshes. The impact of mesh density on results is estimated based on a comparison of the jet diameters at three different locations: at the nozzle outlet, 0.5 and 1.0 mm from the nozzle outlet in the downstream direction.

Figure 4 shows changes in the jet diameter at three different locations as a function of the elementary cell size ratio. The cell size ratio is the ratio between the edge length of the elementary cell in mesh D (5.0 μm) and different meshes (A. B, C and D see Table 3). As can be seen, the average jet diameter converges to the final value at all three locations by refining the elementary cell size. Our jet diameter results are thus independent of the mesh density and size for meshes B-D. Mesh D (cell size ratio 1.0) is used in all further calculations.

3. Experimental setup

The following measurements are performed for validation of the numerical model. The laboratory test rig is shown in Figure 5. A simple GDVN (A) is mounted on a triaxial translational stage (E). The gas is supplied from a pressure tank (J) and controlled via EL-Flow series thermal mass flow controller (I) from Bronkhorst High-Tech Instruments. A pressure drop supplied to the GDVN is measured by a differential pressure sensor Amphenol ELV series. The water flow is metered with a syringe pump Harvard Apparatus Pump 11 elite (G). In the GDVN (A), water is focused and ejected vertically downward in a view window of the SpeedCam Visario high-speed camera by Weinberger (C). The image magnification and focus are achieved using a modular long-distance microscope Optem Fusion by Edmund optics (B). Back illumination by optical fibre is aligned with the camera's optical path and connected to the light source Olympus ILK-5 (D).

The GDVN is printed by the KUDO3D Micro SLA printer. Printing a nozzle with the 0.6 mm orifice diameter takes $\sim$ 4 h.

Mesh	Nr. of cells	Nr. of cells ratio	Min. cell size in x direction [μm]	Min. cell size in y direction [μm]	Min. cell size in z direction [μm]	Nr. of cells across the $D_{j,avg}$
A	2,736,084	0.25	8.33	8.33	8.33	11 (10.8)
B	5,916,786	0.54	6.25	6.25	6.25	14 (14.2)
C	8,224,138	0.74	5.56	5.56	5.56	16 (16.0)
D	11,055,127	1.00	5.00	5.00	5.00	18 (18.2)

Source: Table by authors

Table 3. Properties of different types of meshes

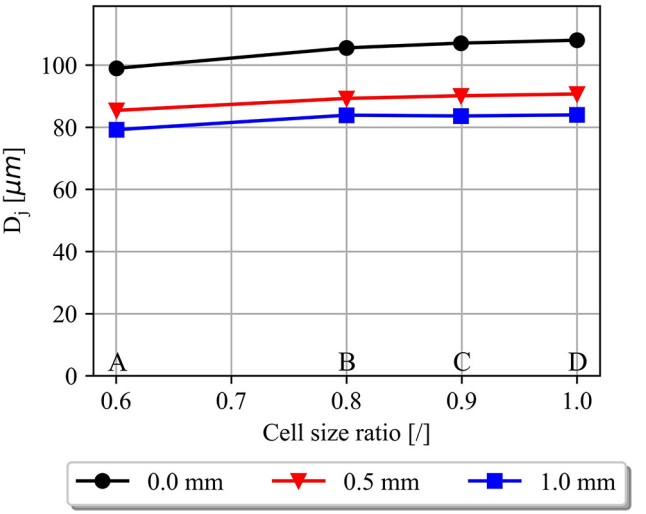

Source: Figure by authors

Figure 4.
Average jet diameter at 0.0, 0.5 and 1.0 mm from the nozzle outlet, calculated with different types of meshes (A–D)

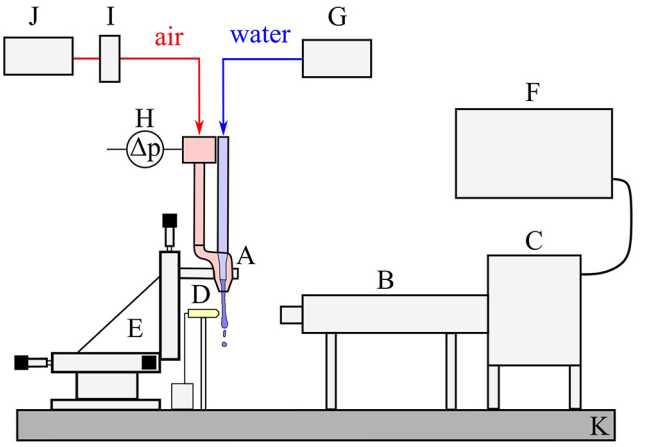

Notes: (A) Nozzle; (B) optical lens; (C) highspeed video camera; (D) source of light; (E) triaxial translation stage; (F) PC; (G) syringe pump; (H) differential pressure sensor; (I) thermal flowmeter; (J) compressed air supply; (K) optical table
Source: Figure by authors

Figure 5.
Experimental setup

3.1 Video analysis

The video samples are recorded in 1536 × 1024 px resolution at 1,000 Hz. A total of 500 frames are analysed for every volumetric flow rate combination.

We recorded animations and videos of the jet's behaviour with data from numerical simulations and experimental measurements, respectively. A purpose-built code, which

analyses jet length and diameter with statistical values, such as average, minimum and maximum values, standard deviation and skewness, is developed in Python using the cv2 library. The video analysing process is divided into four main steps:

(1) frames are extracted from the video;

(2) frames are subtracted with the background frame and binarised from greyscale into black-white images (black has a pixel value of 0 and white a value of 255) using the Otsu threshold method (Otsu, 1979);

(3) the reference object is measured with the code to determine the mm-to-pixel ratio; and

(4) the jet object is recognised from the frame and analysed.

4. Results and discussion

The employed half-space 3D model requires about 30 h of CPU to calculate the steady–state airflow. Meanwhile, about 20–30 days of CPU are required for two-phase flow transient calculation. A total of 72 cores on HPC have been booked for the described analyses.

4.1 Validation of numerical results

The numerical results are compared with the experiment under the same process conditions. Figure 6 shows how the jet diameter, measured experimentally, varies at specific locations (a, b, c) from the nozzle outlet with time. Table 4 shows values of average jet diameter and the discrepancy between the numerical and experimental results at different locations outside the nozzle.

Numerical and experimental results of average jet diameter at different locations match between 2.6% and 5.8%, whereas the jet length is usually longer in the numerical cases. In the case of a physical experiment, we measured average jet lengths 1.74 mm. The calculated average jet length of stabilised numerical solution of 2.93 mm overshoots the experimental data by 68%. The reason for the discrepancy with great merit originates from the fact that the experimental conditions do not experience ideal conditions, and that the jet breakup is a complex non-periodic and multiparametric phenomenon. For an accurate jet length calculation, all influential parameters have to be taken into account within the representative statistical sampling in time. From Figure 7, it seems that our numerical model should be calculated over a longer time period to have a similar density distribution to the experimental jet lengths. We

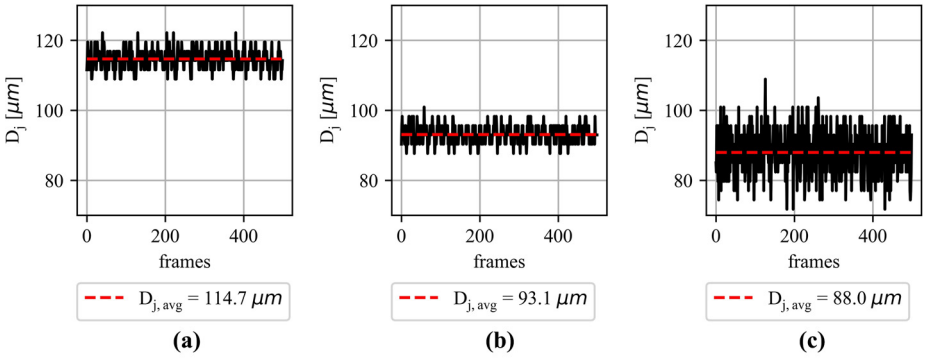

Figure 6. Variation of jet diameter at (a) nozzle outlet; (b) 0.5 mm and (c) 1.0 mm from the nozzle outlet, at G40L1000 and 1536 × 1024 px resolution and 1,000 Hz frequency rate of a highspeed camera

Source: Figure by authors

expect that with further calculation and additional refinement around the jet breakup area, the peak of the calculated jet length distribution might be closer to the experimental one. An accurate jet length calculation is highly challenging, and therefore, up to now, only studies of Zahoor *et al.* (2019) and Nazari *et al.* (2023) provide a comparison of jet length between experiments and simulations.

Also, the statistical samples of the numerical calculations and experiment are different, because of the different timestep size between the frames of numerical animation and experimental video (2 μs vs 1 ms). However, the number of analysed frames is almost the same in numerical simulations (513) and experiment (500). Not exactly the same statistical sample of numerical simulations and experiment have an unneglectable impact on the statistical average of jet length. If the jet lengths are compared as a histogram, a region exists where higher experimental and lower numerical jet lengths overlaps, shown in Figure 7 with the hatched area.

Our numerical model, therefore, correctly predicts the jet length within a range, shown in Figure 7, but overestimates it on an average by 68%. The achieved matching is better than

Table 4.
Error between the numerical and experimental average jet diameters at nozzle outlet, 0.5 and 1.0 mm further downstream from the nozzle outlet for G40L1000 flow rate combination and mesh D

Q_g [L h^{-1}]	Q_l [μL min^{-1}]	Location [mm]	Experimental $D_{j,avg}$ [μm]	Numerical $D_{j,avg}$ [μm]	Error [%]
40	1,000	0.0	114.7	108.0	5.8
40	1,000	0.5	93.1	90.7	2.6
40	1,000	1.0	88.0	84.0	4.5

Source: Table by authors

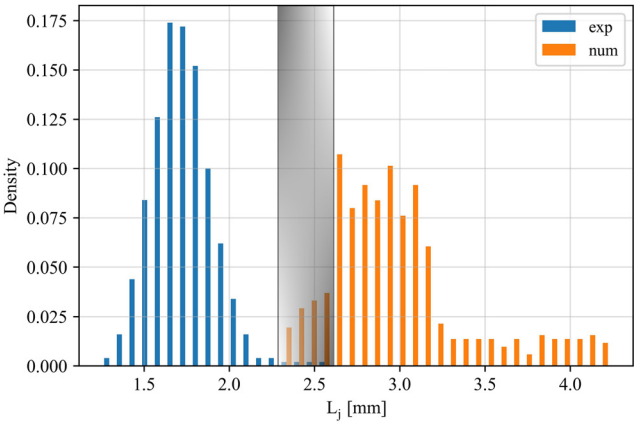

Note: The grey area shows the overlapping between experimental and numerical jet lengths
Source: Figure by authors

Figure 7.
Histogram of the jet length comparison between experimental and numerical results of jetting (G40L1000) regime

in the axisymmetric numerical study by Zahoor *et al.* (2019), where the jet length is overestimated by 89% on average at five process conditions A recent study by Nazari *et al.* (2023) predicts jet lengths with a relative error of 10%. It suggests implementing an adaptive mesh refinement algorithm to calculate jet length accurately. However, in the study of Nazari *et al.* (2023), only the jet length has been validated, but not the jet diameter, as it is also in the present study.

In other investigations of FF jetting regime, scholars mainly validated their numerical model by comparing only the shapes of the fluid entities (Mu *et al.*, 2018b; Wu *et al.*, 2017; Zahoor *et al.*, 2018a) or sometimes jet diameter (Rahimi *et al.*, 2020; Zahoor *et al.*, 2018a; Zhao *et al.*, 2019a, 2019b) or jet velocity (Zahoor *et al.*, 2018a). Jet length is a highly transient parameter compared to the jet diameter, and thus, it is difficult to predict it correctly. However, for the SFX, where the GDVN is most commonly used, the jet length prediction of the jetting regime is less important than the jet diameter prediction if the jets are also with the overestimation significantly longer than a minimum required stable jet length (50 μm or 500 μm on ten times scaled-up model), where the XFEL hits the stable jet. The predicted variation of local jet diameter indicates Plateau–Rayleigh instability which potentially causes the jet breakup.

A more accurate comparison could be made with a higher frequency rate of a high-speed camera and, thus, a direct comparison of experimental and numerical jet length variation for every numerical timestep. In this case, a jet length development could be analysed temporally and not just as a global statistical average.

A half-space 3D model and a spatial discretisation of control volumes have a significant impact on a numerical calculation of jet length. In our fluid domain, cell size grows from a nozzle outlet in a downstream direction. In the area where the jet breaks up, the control volumes should be refined even more in the downstream direction to calculate the interface between air and water accurately. We assume that a complete 3D model should calculate jet length more precisely.

We have also validated the numerical model by comparing gas pressure drop values in the GDVN. The pressure drop has been measured between the connecting tube of the GDVN and the surrounding air [Figure 5(h)]. The numerical values have been calculated by area-weighted average on six (three in radial and three in axial direction) different planes inside the GDVN. Experimentally measured versus numerically calculated pressure drops are 10.1 vs 9.8, 25.0 vs 25.7 and 54.3 vs 55.7 mbar for dripping (G25L500), jetting (G40L1000) and whipping (G60L1000), respectively. Results match within 3% for all three cases.

4.2 Velocity profiles of steady–state simulation

An essential benefit of using half-space 3D numerical simulation compared to axisymmetric one is a more realistic description of the velocity profile caused by the complex printed 3 D nozzle geometry. Figure 8(a) and Figure 8(b) show velocity profiles for the gas phase in terms of velocity magnitude and of u, v and w velocity components inside the nozzle's mixing zone (a) and at the nozzle outlet (b), respectively. The velocities are calculated in a steady-state simulation and used as an initial condition in a two-phase flow transient simulation. It is clearly seen that the velocity profiles calculated with 3D numerical simulation are not close to symmetrical in x direction as prescribed in axisymmetric numeric simulation. Also, the w component of velocity does not take the parabolic profile inside the nozzle. The turn in the GDVN has an evident influence on airflow, leading to the conclusion that the left part of the nozzle has a higher average velocity than the right one. This impacts the jet behaviour because the FF gas acts on one side of the jet with a higher velocity than on the other, and the jet thus declines from the vertical axis for a certain angle.

4.3 Numerical results of flow patterns

The isosurfaces with a volume fraction of 0.5 (air-water interface) at a selected time step for the cases G25L500 (dripping), G40L1000 (jetting) and G60L1000 (whipping) are shown in Figure 9. For a better representation, a mirrored solution of a half-sectioned fluid domain is also displayed. In the dripping regime [Figure 9(a)], a separation of the droplet from the liquid meniscus occurs inside the nozzle before the orifice. In the jetting regime [Figure 9(b)], the first part of the liquid jet, emitting from the meniscus, is stable. Further downstream appear Plateau–Rayleigh (Rayleigh, 1878) instabilities, leading to the jet breaking into droplets. In the whipping regime [Figure 9(c)], oscillations from the central axis of the jet are observed, which propagate downstream and lead to a jet breakup.

4.4 Numerical and experimental flow patterns

The numerical data is recorded every 2 μs for a total physical time of approximately 6 ms, and the frequency rate of a high-speed camera is 1000 Hz. The numerical values of the jet behaviour can thus not be compared with the experimental data at each numerical record due to the lack of more frequent experimental frames. However, the flow regimes from the numerical solution correspond perfectly with the experimentally observed flow regimes at the same combination of air and water volumetric flow rates. The same jet shapes can be found in both physical and numerical experiments, as shown in Figure 10. A part of the nozzle outlet is added to the numerical solution for a better representation. The experimental and numerical frames are at the same scale.

In the dripping regime [Figure 10(a)], the same distribution of the droplets with similar distances between them has been found in comparing numerical with experimental results. The droplet size near the nozzle outlet in simulations also matches the experiment. Further downstream, the numerically calculated droplet size is smaller than the experimentally observed. The droplets in the experiment are not falling at the centre of the nozzle axis; therefore, they seem to be larger because they are falling at a certain angle, declined from the axis and are closer to the camera window. This can be concluded from the experimental frame, where the droplet at the nozzle outlet is focused more than the droplet far from the nozzle, since the focus of the high-speed camera was set to nozzle's symmetry plane. Our half-space 3D numerical model does not allow us to simulate a declination perpendicular to the ZX (nozzle's symmetry) plane. With the complete 3D model, the droplets' size far from the nozzle would be more similar to the droplet size in experimental frames. The appearance of the satellite droplet is not precisely at the same

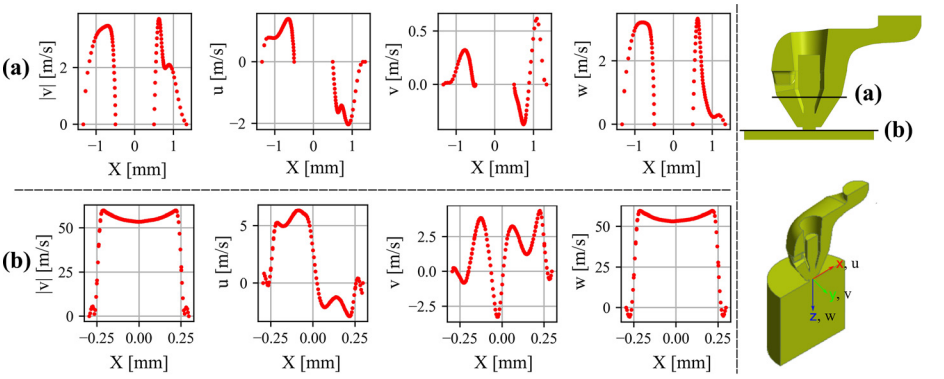

Figure 8.
Velocity profiles of magnitude |v| and u, v, and w components for mesh D at (a) 1.3 mm inside the nozzle and (b) nozzle outlet

Source: Figure by authors

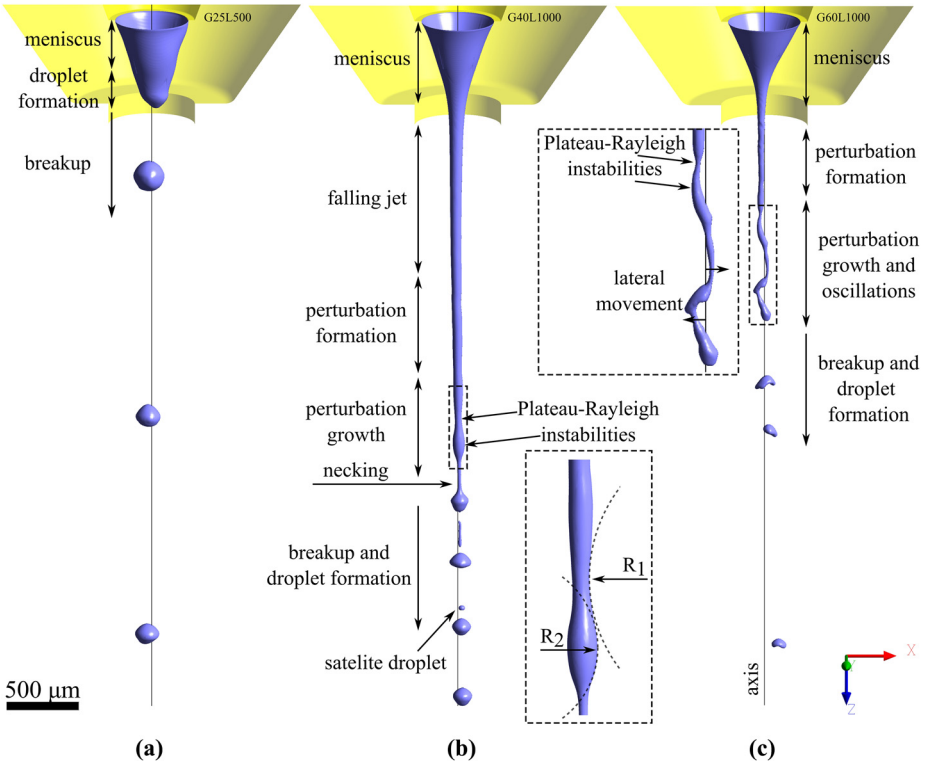

Source: Figure by authors

Figure 9.
Isosurface of volume fraction of 0.5 for (a) dripping; (b) jetting and (c) whipping regime

location, but the existence of the satellite droplet from numerical simulation has been confirmed by experimental recording. In Figure 10(a), arrows are pointing at the satellite droplets.

In the jetting regime [Figure 10(b)], the matching shapes have been found in experimental and numerical frames. The jet breakup process on those frames is the same as the number of Plateau–Rayleigh instabilities. The length of the jet is significantly longer in numerical frames than in the experimental ones. The reasons for the discrepancy are discussed in Section 4.1.

In the whipping regime [Figure 10(c)], the same jet shapes can be recognised in experimental and numerical frames with the same number of regions where Plateau–Rayleigh instability occurs. A similar declination from the central axis line is also observed.

It can be concluded that the developed numerical model can predict realistic behaviour and shapes of jets and droplets for dripping, jetting and whipping regimes.

4.5 Flow pattern map

Figure 11 shows the flow pattern diagram of different flow regimes observed experimentally. The flow patterns can be sorted into four main groups: jetting, whipping, dripping and spurting. Different regimes are delineated with subjectively determined borders. On the same diagram, the corresponding numerical simulations are plotted. For the cases G25L500

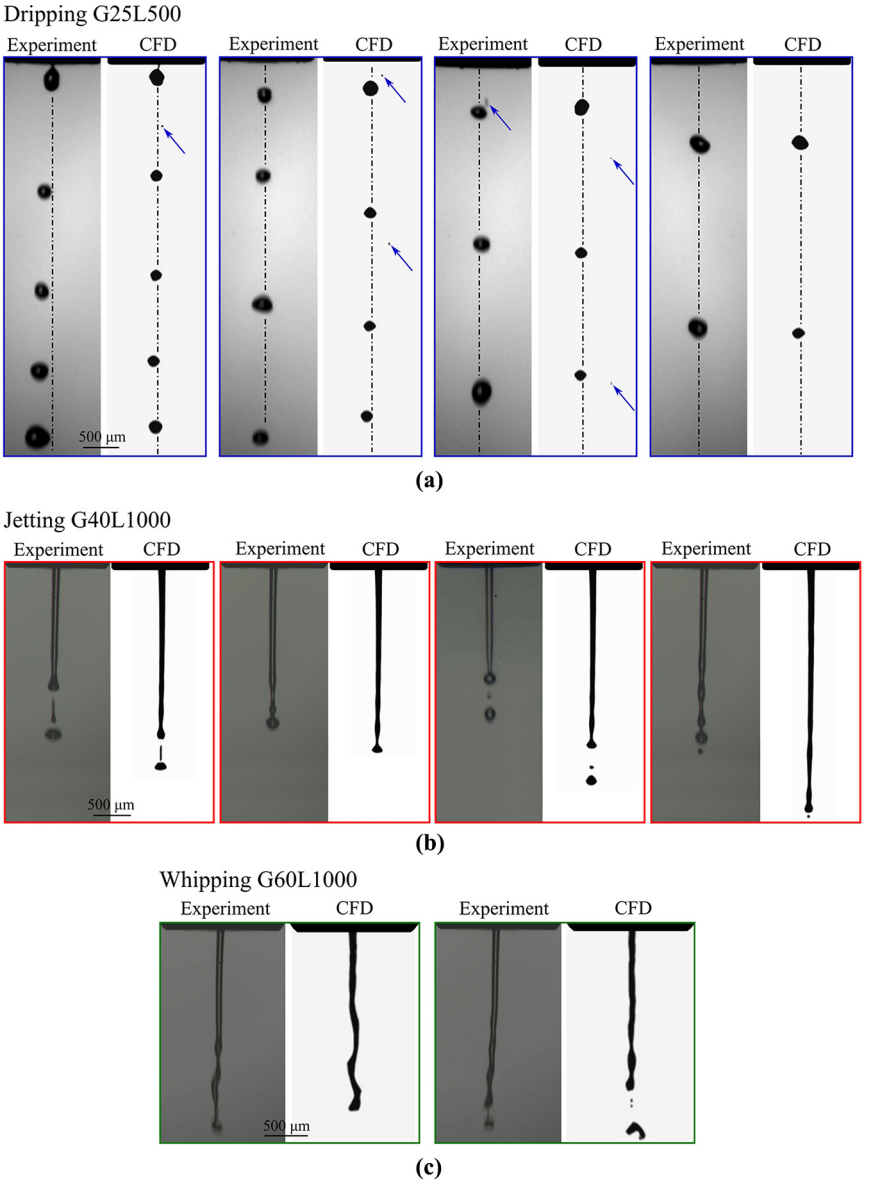

Figure 10.
A comparison of experimental vs numerical jet shapes for (a) dripping G25L500; (b) jetting G40L1000 and (c) whipping G60L1000

Note: Figures are of the same ratio with the scale bar specified for each flow regime. Arrows point to the satellite droplets
Source: Figure by authors

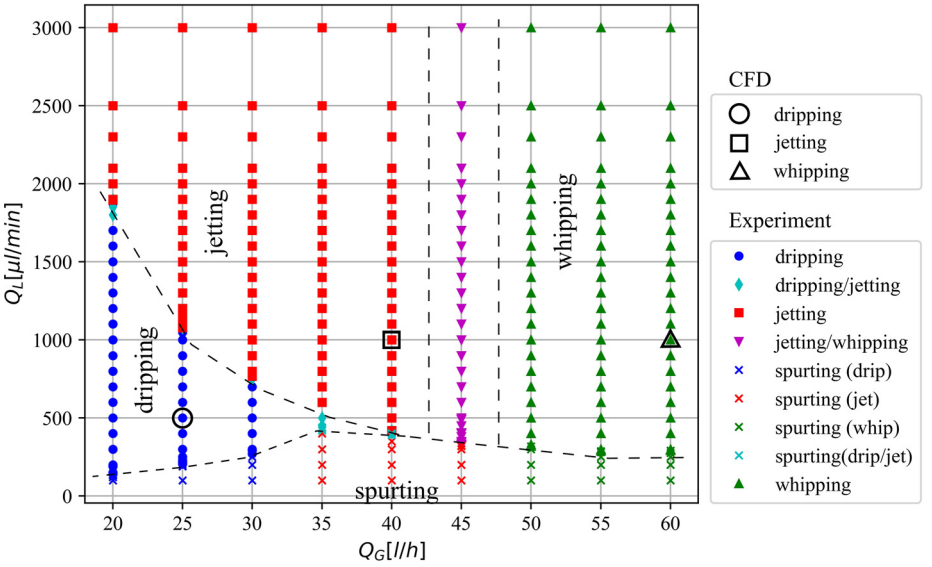

Note: Experimental and numerical jet modes
Source: Figure by authors

Figure 11.
Flow pattern map

(dripping), G40L1000 (jetting) and G60L1000 (whipping), the numerical flow regimes perfectly match the experimental ones.

4.6 Velocity

As VOF model calculates only the mixture velocity field of both, liquid and gas phase, we split the velocity field at the water volume fraction greater or equal to 0.5 to show the velocity of the liquid jet. The jet surface moves faster than the liquid jet core, as the gas is acting on the jet surface and transferring momentum to it. Therefore, the impact of the focusing gas is more significant on the surface since the gas accelerates the fluid at the surface more than at the jet's core. The gas flow around the jet changes over time, influencing the jet breakup (see Section 4.7). Both the jet core and surface are accelerating downstream, but the acceleration of the jet core is delayed. This delay can be seen in Figure 12, where the plots of jet core velocity magnitude and water volume fraction versus x coordinate at the nozzle outlet, 0.5 and 1.0 mm further downstream, are plotted. The jet's surface and core velocities ratio is around 1.7, 1.5 and 1.25 at the nozzle outlet, 0.5 and 1.0 mm downstream, respectively. Obviously, the momentum from the focusing gas is transferred faster to the jet's surface than to its core. When the transferred momentum from the focusing gas reaches the liquid core, the difference between the jet surface and core velocities decreases in the downstream direction. The plots in Figure 12 show that the jet slightly declined to the left. Also, the jet velocity minimum is slightly moved in the left direction. The reason is the slightly different velocity distribution of surrounding gas, which transfers momentum asymmetrically regarding the jet axis, leading to the jet and jet velocity minimum declination. Owing to the increased jet velocity, the jet diameter decreases downstream to satisfy the volume (mass) flux conservation condition. An example of determining the jet diameter from the plot in Figure 12 is shown for the middle timestep.

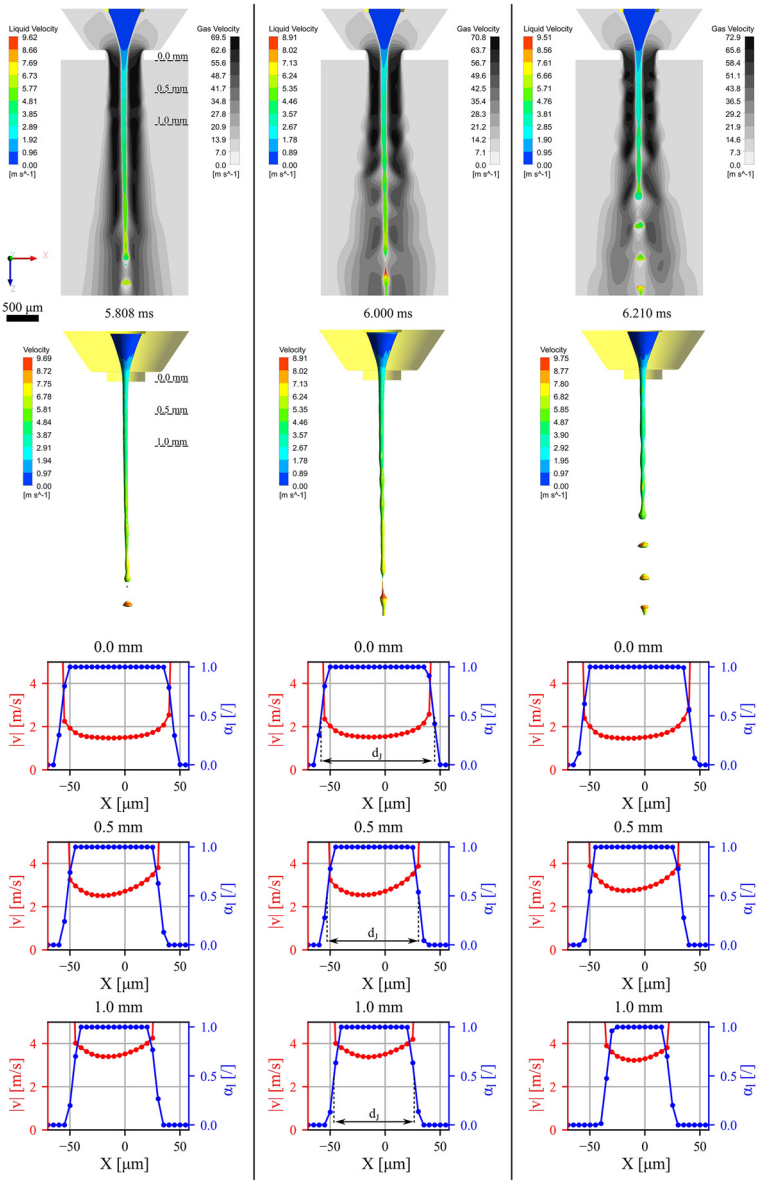

Note: An example of how to obtain the jet diameter is shown at the middle timestep

Source: Figure by authors

Figure 12.
Velocity field of the liquid jet core (top) and surface (middle) and charts of jet core velocity magnitude vs X coordinate for the jetting regime at three different locations during three different timesteps

4.7 Kinetic energy transfer

Volume-specific kinetic energy is calculated as

$$e_{k,\alpha} = \frac{E_{k,\alpha}}{V} = \alpha \frac{1}{2} \rho_\alpha |v|^2 \tag{13}$$

where α stands for volume fraction, ρ for density, $|v|$ for velocity magnitude and V for the cell volume. The volume-specific kinetic energy represents a dynamic pressure of the individual phase as also of the mixture in the two-phase transitional area ($0 < \alpha < 1$), where it is weighted according to the volume fraction value.

In flow-focusing, a given total energy of the gas, expressed as a total pressure of the gas is first transformed to the dynamic pressure in the nozzle orifice region. Here dynamic pressure of the focusing gas arises, as also the kinetic energy, which is transferred to the liquid phase during the downstream flow. Thus, the kinetic energy of the gas decreases, and the liquid's kinetic energy increases downstream from the nozzle outlet. The energy transfer process is continuous and occurs at all fluid entities, also after the breakup.

The volume-specific kinetic energy of air and water at a time instance is shown in Figure 13 for dripping [13(a)], jetting [13(b)] and whipping regimes [13(c)], respectively. In all regimes, locations with increased values of the specific kinetic energy of gas are observed. In the jetting regime, these locations are almost symmetrical across the jet axis, whereas in the whipping regime, the locations are evidently unsymmetrical. These local areas act with locally higher dynamic pressure on a liquid jet. At these locations, the liquid jet is focused more, resulting in a locally narrower jet diameter, known as necking or Plateau–Rayleigh instability. Therefore, focusing gas increases Plateau–Rayleigh instabilities, which are always present in any kind of the jet, apart from FF. In the whipping regime, locations with increased specific kinetic energy are distributed unsymmetrically. This results in asymmetric dynamic pressure distribution, and the jet declines towards the area with locally decreased specific kinetic energy.

The reason of the areas with the locally increased dynamic pressure of the gas could originate from the decreased cross-section of the airflow due to the locally increased liquid jet volume due to the increase in jet diameter, which occupies the space of the gas phase flow. This could be well seen in the dripping regime, where the locally increased areas of dynamic gas pressure generated at the droplet detaching point. The process is equivalent to the flow around the cylinder, including the wake region behind the droplet. The occurrence of the locally increased regions of dynamic gas pressure in the jetting and whipping regime could be induced by the change in airflow around the PR instabilities of the liquid jet stream. Where the streamlines of the gas flow are focused together, its cross section is lower and thus, higher velocity (specific kinetic energy) occurs in this region, seen in Figure 14. These regions are visible in Figure 13(b) around the thickened region of the liquid jet.

5. Conclusions

This investigation focused on developing the half-space 3D numerical simulation of the GDVN, its experimental validation and assessing its capabilities towards the axisymmetric simulation. Three gas and liquid volumetric flow rate combinations are simulated to calculate dripping, jetting and whipping regimes, experimentally observed at certain flow rate combinations. A comparison between experimental and numerical snapshots of jet shapes and structures are analysed. The same jet shapes are observed in numerical and experimental approaches for dripping, jetting and whipping flow regimes. For the jetting regime, it is shown that average jet diameters at different locations agree well with the experimental results, differing at most 5.8%. A simulated gas pressure drop in dripping,

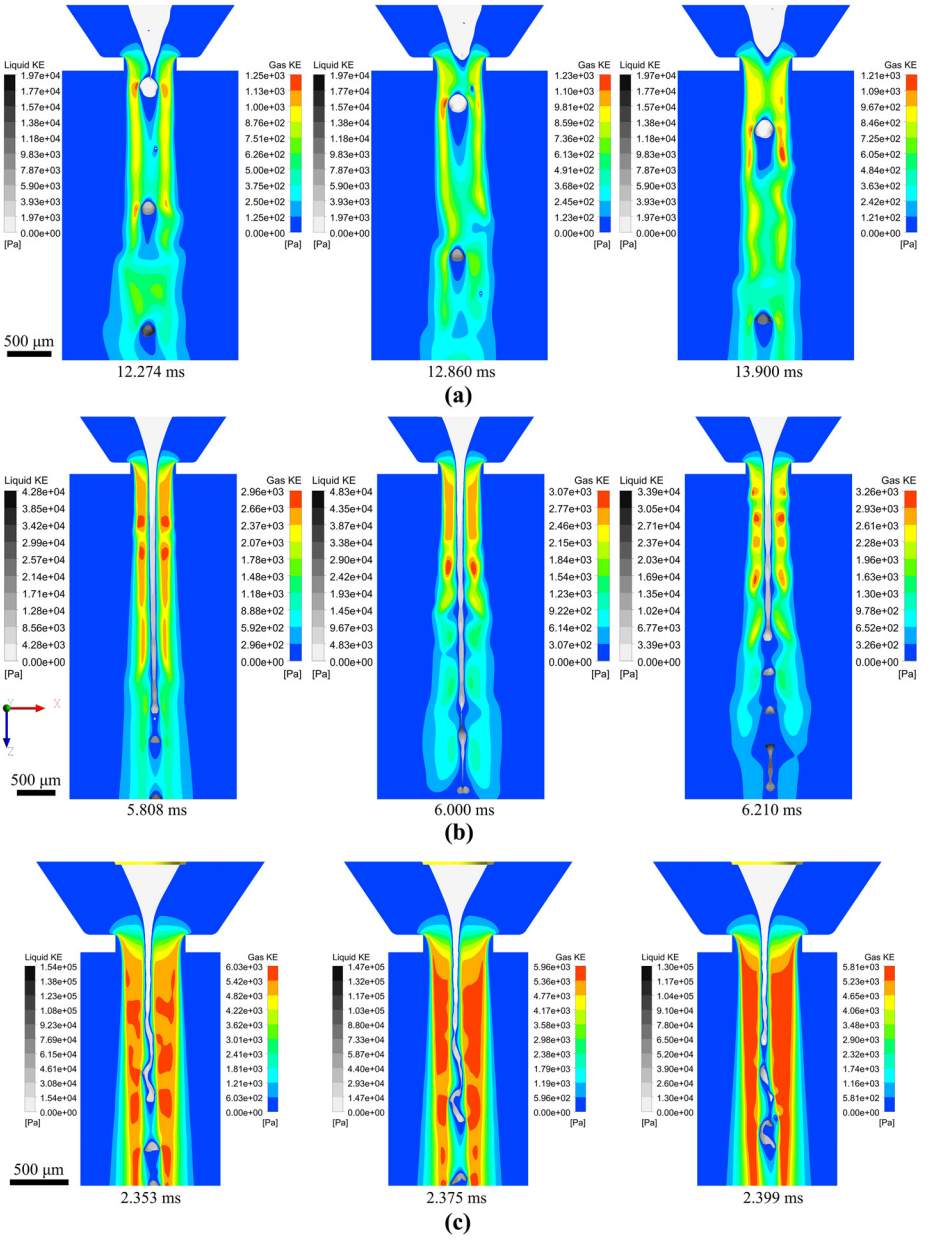

Figure 13.
Specific kinetic energy of air and water for (a) dripping G25L500; (b) jetting G40L1000 and (c) whipping G60L1000 regime

Source: Figure by authors

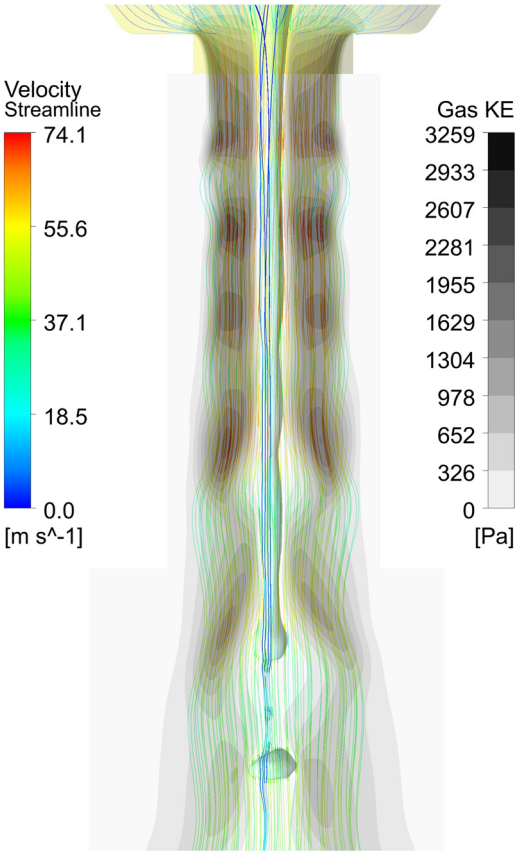

Source: Figure by authors

Figure 14.
Streamlines of velocity and volume-specific kinetic energy (dynamic pressure) field for jetting (G40L1000)

jetting and whipping regimes matches within 3% of the experimental results. However, the model has difficulties with jet length calculation, which is less important than the accurate jet diameter calculation in the most widely used application of SFX. For SFX jet diameter prediction close to the nozzle outlet is a key parameter.

The main advantage of the half-space 3D model over the axisymmetric one is the possibility of including the nozzle geometry's influence on the flow and allowing the simulation of the whipping flow regime with a lateral movement of the jet around the jet axis. This model allows realistic jet behaviour, including fine jet declinations from the axis due to the non-axisymmetrical velocity field of the focusing gas.

The numerical model does not provide accurate results of the jet length. Its physics could be improved by considering the entire 3D model on the expense of more than double computing time.

With a higher resolution of high-speed camera, the experimental measurements of the jet diameters and lengths would be more accurate. With a higher frequency rate of frames

filmed with a high-speed camera the numerical results and experimental measurements can be compared temporarily, not just with the average jet diameter and length values.

Nevertheless, the presented model is adequate for modelling most typical flow modes of GDVN.

References

Acero, A.J., Montanero, J.M., Ferrera, C., Herrada, M.A. and Gañán-Calvo, A.M. (2012), "Enhancement of the stability of the flow focusing technique for low-viscosity liquids", *Journal of Micromechanics and Microengineering*, Vol. 22 No. 11, p. 115039, doi: 10.1088/0960-1317/22/11/115039.

Aghaei, H., Solaimany Nazar, A.R. and Varshosaz, J. (2021), "Double flow focusing microfluidic-assisted based preparation of methotrexate–loaded liposomal nanoparticles: encapsulation efficacy, drug release and stability", *Colloids and Surfaces A: Physicochemical and Engineering Aspects*, Vol. 614, p. 126166, doi: 10.1016/j.colsurfa.2021.126166.

Anna, S.L., Bontoux, N. and Stone, H.A. (2003), "Formation of dispersions using 'flow focusing' in microchannels", *Applied Physics Letters*, Vol. 82 No. 3, pp. 364-366, doi: 10.1063/1.1537519.

Belšak, G., Bajt, S. and Šarler, B. (2021), "Computational modeling and simulation of gas focused liquid micro-sheets", *International Journal of Multiphase Flow*, Vol. 140, p. 103666, doi: 10.1016/j.ijmultiphaseflow.2021.103666.

Beyerlein, K.R., Adriano, L., Heymann, M., Kirian, R., Knoška, J., Wilde, F., Chapman, H.N. and Bajt, S. (2015), "Ceramic micro-injection molded nozzles for serial femtosecond crystallography sample delivery", *Review of Scientific Instruments*, Vol. 86 No. 12, p. 125104, doi: 10.1063/1.4936843.

Blanco-Trejo, S., Herrada, M.A., Gañán-Calvo, A.M., Rubio, A., Cabezas, M.G. and Montanero, J.M. (2020), "Whipping in gaseous flow focusing", *International Journal of Multiphase Flow*, Vol. 130, p. 103367, doi: 10.1016/j.ijmultiphaseflow.2020.103367.

Cabezas, M.G., Rebollo-Muñoz, N., Rubio, M., Herrada, M.A. and Montanero, J.M. (2021), "Global stability analysis of axisymmetric liquid–liquid flow focusing", *Journal of Fluid Mechanics*, Vol. 909, p. A10, doi: 10.1017/jfm.2020.953.

Chapman, H.N., Fromme, P., Barty, A., White, T.A., Kirian, R.A., Aquila, A., Hunter, M.S., Schulz, J., DePonte, D.P., Weierstall, U. and Doak, R.B. (2011), "Femtosecond X-ray protein nanocrystallography", *Nature*, Vol. 470 No. 7332, pp. 73-77, doi: 10.1038/nature09750.

Chen, Y., Wu, L. and Zhang, L. (2015), "Dynamic behaviors of double emulsion formation in a flow-focusing device", *International Journal of Heat and Mass Transfer*, Vol. 82, pp. 42-50, doi: 10.1016/j.ijheatmasstransfer.2014.11.027.

Chen, Q., Li, J., Song, Y., Chen, B., Christopher, D.M. and Li, X. (2021), "Pressure-driven microfluidic droplet formation in Newtonian and shear-thinning fluids in glass flow-focusing microchannels", *International Journal of Multiphase Flow*, Vol. 140, p. 103648, doi: 10.1016/j.ijmultiphaseflow.2021.103648.

Cruz-Mazo, F., Herrada, M.A., Gañán-Calvo, A.M. and Montanero, J.M. (2017), "Global stability of axisymmetric flow focusing", *Journal of Fluid Mechanics*, Vol. 832, pp. 329-344, doi: 10.1017/jfm.2017.684.

DePonte, D.P., Weierstall, U., Schmidt, K., Warner, J., Starodub, D., Spence, J.C.H. and Doak, R.B. (2008), "Gas dynamic virtual nozzle for generation of microscopic droplet streams", *Journal of Physics D: Applied Physics*, Vol. 41 No. 19, p. 195505, doi: 10.1088/0022-3727/41/19/195505.

Dewandre, A., Rivero-Rodriguez, J., Vitry, Y., Sobac, B. and Scheid, B. (2020), "Microfluidic droplet generation based on non-embedded co-flow-focusing using 3D printed nozzle", *Scientific Reports*, Vol. 10 No. 1, p. 21616, doi: 10.1038/s41598-020-77836-y.

Duan, H., Romay, F.J., Li, C., Naqwi, A., Deng, W. and Liu, B.Y.H. (2016), "Generation of monodisperse aerosols by combining aerodynamic flow-focusing and mechanical perturbation", *Aerosol Science and Technology*, Vol. 50 No. 1, pp. 17-25, doi: 10.1080/02786826.2015.1123213.

Evangelio, A., Campo-Cortés, F. and Gordillo, J.M. (2016), "Simple and double microemulsions via the capillary breakup of highly stretched liquid jets", *Journal of Fluid Mechanics*, Vol. 804, pp. 550-577, doi: 10.1017/jfm.2016.498.

Fluent, A. (2020), "Ansys fluent 2020 R1-Theory guide; user's guide", Canonsburg, PA, USA.

Gañán-Calvo, A.M. (1998), "Generation of steady liquid microthreads and micron-sized monodisperse sprays in gas streams", *Physical Review Letters*, Vol. 80 No. 2, pp. 285-288, doi: 10.1103/PhysRevLett.80.285.

Gañán-Calvo, A.M., Montanero, J.M., Martín-Banderas, L. and Flores-Mosquera, M. (2013), "Building functional materials for health care and pharmacy from microfluidic principles and flow focusing", *Advanced Drug Delivery Reviews*, Vol. 65 Nos 11/12, pp. 1447-1469, doi: 10.1016/j.addr.2013.08.003.

Guimarães, C.F., Gasperini, L., Marques, A.P. and Reis, R.L. (2021), "3D flow-focusing microfluidic biofabrication: one-chip-fits-all hydrogel fiber architectures", *Applied Materials Today*, Vol. 23, p. 101013, doi: 10.1016/j.apmt.2021.101013.

Han, W., Chen, X., Wu, Z. and Zheng, Y. (2019), "Three-dimensional numerical simulation of droplet formation in a microfluidic flow-focusing device", *Journal of the Brazilian Society of Mechanical Sciences and Engineering*, Vol. 41 No. 6, p. 265, doi: 10.1007/s40430-019-1767-y.

Herrada, M.A., Gañán-Calvo, A.M., Ojeda-Monge, A., Bluth, B. and Riesco-Chueca, P. (2008), "Liquid flow focused by a gas: jetting, dripping, and recirculation", *Physical Review E*, Vol. 78 No. 3, p. 36323, doi: 10.1103/PhysRevE.78.036323.

Hua, J., Zhang, B. and Lou, J. (2007), "Numerical simulation of microdroplet formation in coflowing immiscible liquids", *AIChE Journal*, Vol. 53 No. 10, pp. 2534-2548, doi: 10.1002/aic.11287.

Huang, J. and Yao, Z. (2022), "Influencing factors and size prediction of bubbles formed by flow focusing in a cross-channel", *Chemical Engineering Science*, Vol. 248, p. 117228, doi: 10.1016/j.ces.2021.117228.

Inguva, V., Graceffa, R., Schulz, J., Bilsel, O. and Perot, B.J. (2019), "Creating round focused micro-jets from rectangular nozzles", *Journal of Mechanical Science and Technology*, Vol. 33 No. 9, pp. 4281-4289, doi: 10.1007/s12206-019-0824-x.

Jafari, A. and Shamloo, A. (2023), "CFD study of droplet formation in a cross-junction microfluidic device: investigating the impact of outflow channel design and viscosity ratio", *Engineering Applications of Computational Fluid Mechanics*, Vol. 17 No. 1, p. 2243091, doi: 10.1080/19942060.2023.2243091.

Jensen, M.J., Stone, H.A. and Bruus, H. (2006), "A numerical study of two-phase stokes flow in an axisymmetric flow-focusing device", *Physics of Fluids*, Vol. 18 No. 7, doi: 10.1063/1.2214461.

Khater, A., Abdelrehim, O., Mohammadi, M., Mohamad, A. and Sanati-Nezhad, A. (2021), "Thermal droplet microfluidics: from biology to cooling technology", *TrAC Trends in Analytical Chemistry*, Vol. 138, p. 116234, doi: 10.1016/j.trac.2021.116234.

Khater, A., Abdelrehim, O., Mohammadi, M., Azarmanesh, M., Janmaleki, M., Salahandish, R., Mohamad, A. and Sanati-Nezhad, A. (2020), "Picoliter agar droplet breakup in microfluidics meets microbiology application: numerical and experimental approaches", *Lab on a Chip*, Vol. 20 No. 12, pp. 2175-2187, doi: 10.1039/D0LC00300J.

Klimešová, E., Kulyk, O., Hoque, Z., Roos, A.H., Khakurel, K.P., Rebarz, M., Jurkovičová, L., Albrecht, M., Finke, O., Lera, R. and Hort, O. (2021), "A multipurpose end-station for atomic, molecular and optical sciences and coherent diffractive imaging at ELI beamlines", *The European Physical Journal Special Topics*, Vol. 230 No. 23, pp. 4183-4194, doi: 10.1140/epjs/s11734-021-00192-z.

Knoška, J., Adriano, L., Awel, S., Beyerlein, K.R., Yefanov, O., Oberthuer, D., Peña Murillo, G.E., Roth, N., Sarrou, I., Villanueva-Perez, P. and Wiedorn, M.O. (2020), "Ultracompact 3D microfluidics for time-resolved structural biology", *Nature Communications*, Vol. 11 No. 1, p. 657, doi: 10.1038/s41467-020-14434-6.

Mamet, V., Namy, P. and Dedulle, J.M. (2017), "Numerical modeling of flow focusing: quantitative characterization of the flow regimes", *Physics of Fluids*, Vol. 29 No. 9, doi: 10.1063/1.5003840.

Mu, K., Ding, H. and Si, T. (2018a), "Instability analysis of the cone–jet flow in liquid-driven flow focusing", *Microfluidics and Nanofluidics*, Vol. 22 No. 12, p. 138, doi: 10.1007/s10404-018-2158-x.

Mu, K., Si, T. and Ding, H. (2019), "Nonlinear dynamics and manipulation of dripping in capillary flow focusing", *Science China Physics, Mechanics and Astronomy*, Vol. 62 No. 12, p. 124713, doi: 10.1007/s11433-019-9444-8.

Mu, K., Ding, H. and Si, T. (2020), "Experimental and numerical investigations on interface coupling of coaxial liquid jets in co-flow focusing", *Physics of Fluids*, Vol. 32 No. 4, doi: 10.1063/5.0002102.

Mu, K., Si, T., Li, E., Xu, R.X. and Ding, H. (2018b), "Numerical study on droplet generation in axisymmetric flow focusing upon actuation", *Physics of Fluids*, Vol. 30 No. 1, doi: 10.1063/1.5009601.

Mühlig, K., Gañán-Calvo, A.M., Andreasson, J., Larsson, D.S.D., Hajdu, J. and Svenda, M. (2019), "Nanometre-sized droplets from a gas dynamic virtual nozzle", *Journal of Applied Crystallography*, Vol. 52 No. 4, pp. 800-808, doi: 10.1107/S1600576719008318.

Müller, T., Sänger, A., Habisreuther, P., Jakobs, T., Trimis, D., Kolb, T. and Zarzalis, N. (2016), "Simulation of the primary breakup of a high-viscosity liquid jet by a coaxial annular gas flow", *International Journal of Multiphase Flow*, Vol. 87, pp. 212-228, doi: 10.1016/j.ijmultiphaseflow.2016.09.008.

Nazari, R., Ansari, A., Herrmann, M., Adrian, R.J. and Kirian, R.A. (2023), "Numerical and experimental investigation of gas flow field variations in three-dimensional printed gas-dynamic virtual nozzles", *Frontiers in Mechanical Engineering*, Vol. 8, p. 958963, doi: 10.3389/fmech.2022.958963.

Nelson, G., Kirian, R.A., Weierstall, U., Zatsepin, N.A., Faragó, T., Baumbach, T., Wilde, F., Niesler, F. B., Zimmer, B., Ishigami, I. and Hikita, M. (2016), "Three-dimensional-printed gas dynamic virtual nozzles for x-ray laser sample delivery", *Optics Express*, Vol. 24 No. 11, pp. 11515-11530, doi: 10.1364/OE.24.011515.

Nguyen, H.Q. and Seo, T.S. (2022), "A 3D printed size-tunable flow-focusing droplet microdevice to produce cell-laden hydrogel microspheres", *Analytica Chimica Acta*, Vol. 1192, p. 339344, doi: 10.1016/j.aca.2021.339344.

Nguyen, N.T., Wereley, S. and Shaegh, S.A.M. (2019), *Fundamentals and Applications of Microfluidics*, 3rd ed., Artech, available at: https://ieeexplore.ieee.org/document/9098772

Nunes, J.K., Tsai, S.S.H., Wan, J. and Stone, H.A. (2013), "Dripping and jetting in microfluidic multiphase flows applied to particle and fibre synthesis", *Journal of Physics D: Applied Physics*, Vol. 46 No. 11, p. 114002, doi: 10.1088/0022-3727/46/11/114002.

Ontiveros, J.F., Company, R., Vaz, M.O. and Nardello-Rataj, V. (2020), "Microfluidic emulsification: process and formulation variables effects in flow behavior pattern on a flow-focusing device", *Colloids and Surfaces A: Physicochemical and Engineering Aspects*, Vol. 601, p. 125038, doi: 10.1016/j.colsurfa.2020.125038.

Otsu, N. (1979), "A threshold selection method from gray-level histograms", *IEEE Transactions on Systems, Man, and Cybernetics*, Vol. 9 No. 1, pp. 62-66, doi: 10.1109/TSMC.1979.4310076.

Pan, D., Chen, Q., Zeng, Y. and Li, B. (2020), "Droplets containing large solid particle inside formation and breakup dynamics in a flow-focusing microfluidic device", *Experimental Thermal and Fluid Science*, Vol. 115, p. 110103, doi: 10.1016/j.expthermflusci.2020.110103.

Ponce-Torres, A., Vega, E.J., Castrejón-Pita, A.A. and Montanero, J.M. (2017), "Smooth printing of viscoelastic microfilms with a flow focusing ejector", *Journal of Non-Newtonian Fluid Mechanics*, Vol. 249, pp. 1-7, doi: 10.1016/j.jnnfm.2017.09.004.

Ponce-Torres, A., Ortega, E., Rubio, M., Rubio, A., Vega, E.J. and Montanero, J.M. (2019), "Gaseous flow focusing for spinning micro and nanofibers", *Polymer*, Vol. 178, p. 121623, doi: 10.1016/j.polymer.2019.121623.

Rahimi, M., Shams Khorrami, A. and Rezai, P. (2019), "Effect of device geometry on droplet size in co-axial flow-focusing microfluidic droplet generation devices", *Colloids and Surfaces A: Physicochemical and Engineering Aspects*, Vol. 570, pp. 510-517, doi: 10.1016/j.colsurfa.2019.03.067.

Rahimi, M., Yazdanparast, S. and Rezai, P. (2020), "Parametric study of droplet size in an axisymmetric flow-focusing capillary device", *Chinese Journal of Chemical Engineering*, Vol. 28 No. 4, pp. 1016-1022, doi: 10.1016/j.cjche.2019.12.026.

Rayleigh, L. (1878), "On the instability of jets", *Proceedings of the London Mathematical Society*, Vol. s1-10 No. 1, pp. 4-13, doi: 10.1112/plms/s1-10.1.4.

Rubio, M., Rubio, A., Cabezas, M.G., Herrada, M.A., Gañán-Calvo, A.M. and Montanero, J.M. (2021), "Transonic flow focusing: stability analysis and jet diameter", *International Journal of Multiphase Flow*, Vol. 142, p. 103720, doi: 10.1016/j.ijmultiphaseflow.2021.103720.

Šarler, B., Zahoor, R. and Bajt, S. (2021), "Alternative geometric arrangements of the nozzle outlet orifice for liquid micro-jet focusing in gas dynamic virtual nozzles", *Materials*, Vol. 14 No. 6, p. 1572, doi: 10.3390/ma14061572.

Segers, T., de Rond, L., de Jong, N., Borden, M. and Versluis, M. (2016), "Stability of monodisperse phospholipid-coated microbubbles formed by flow-focusing at high production rates", *Langmuir, American Chemical Society*, Vol. 32 No. 16, pp. 3937-3944, doi: 10.1021/acs.langmuir.6b00616.

Si, T., Li, F., Yin, X.Y. and Yin, X.Z. (2009), "Modes in flow focusing and instability of coaxial liquid–gas jets", *Journal of Fluid Mechanics*, Vol. 629, pp. 1-23, doi: 10.1017/S0022112009006211.

Si, T., Feng, H., Luo, X. and Xu, R.X. (2015), "Formation of steady compound cone-jet modes and multilayered droplets in a tri-axial capillary flow focusing device", *Microfluidics and Nanofluidics*, Vol. 18 Nos 5/6, pp. 967-977, doi: 10.1007/s10404-014-1486-8.

Si, T., Yin, C., Gao, P., Li, G., Ding, H., He, X., Xie, B. and Xu, R.X. (2016), "Steady cone-jet mode in compound-fluidic electro-flow focusing for fabricating multicompartment microcapsules", *Applied Physics Letters*, Vol. 108 No. 2, doi: 10.1063/1.4939632.

Soroor, M., Zabetian Targhi, M. and Tabatabaei, S.A. (2021), "Numerical and experimental investigation of a flow focusing droplet-based microfluidic device", *European Journal of Mechanics - B/Fluids*, Vol. 89, pp. 289-300, doi: 10.1016/j.euromechflu.2021.06.013.

Trebbin, M., Krüger, K., DePonte, D.P., Roth, S.V., Chapman, H.N. and Förster, S. (2014), "Microfluidic liquid jet system with compatibility for atmospheric and high-vacuum conditions", *Lab Chip*, Vol. 14 No. 10, pp. 1733-1745.

Vasireddi, R., Kruse, J., Vakili, M., Kulkarni, S., Keller, T.F., Monteiro, D.C.F. and Trebbin, M. (2019), "Solution blow spinning of polymer/nanocomposite micro-/nanofibers with tunable diameters and morphologies using a gas dynamic virtual nozzle", *Scientific Reports*, Vol. 9 No. 1, p. 14297, doi: 10.1038/s41598-019-50477-6.

Vega, E.J., Montanero, J.M., Herrada, M.A. and Gañán-Calvo, A.M. (2010), "Global and local instability of flow focusing: the influence of the geometry", *Physics of Fluids*, Vol. 22 No. 6, doi: 10.1063/1.3450321.

Vega, E.J., Acero, A.J., Montanero, J.M., Herrada, M.A. and Gañán-Calvo, A.M. (2014), "Production of microbubbles from axisymmetric flow focusing in the jetting regime for moderate Reynolds numbers", *Physical Review E*, Vol. 89 No. 6, p. 63012, doi: 10.1103/PhysRevE.89.063012.

Wu, L., Liu, X., Zhao, Y. and Chen, Y. (2017), "Role of local geometry on droplet formation in axisymmetric microfluidics", *Chemical Engineering Science*, Vol. 163, pp. 56-67, doi: 10.1016/j.ces.2017.01.022.

Wu, Q., Yang, C., Yang, J., Huang, F., Liu, G., Zhu, Z., Si, T., *et al.* (2018), "Photopolymerization of complex emulsions with irregular shapes fabricated by multiplex coaxial flow focusing", *Applied Physics Letters*, Vol. 112 No. 7, doi: 10.1063/1.5018207.

Yu, C., Wu, L., Li, L. and Liu, M. (2019), "Experimental study of double emulsion formation behaviors in a one-step axisymmetric flow-focusing device", *Experimental Thermal and Fluid Science*, Vol. 103, pp. 18-28, doi: 10.1016/j.expthermflusci.2018.12.032.

Yu, W., Li, B., Liu, X. and Chen, Y. (2021), "Hydrodynamics of triple emulsion droplet generation in a flow-focusing microfluidic device", *Chemical Engineering Science*, Vol. 243, p. 116648, doi: 10.1016/j.ces.2021.116648.

Zahoor, R., Bajt, S. and Šarler, B. (2018a), "Influence of gas dynamic virtual nozzle geometry on micro-jet characteristics", *International Journal of Multiphase Flow*, Vol. 104, pp. 152-165, doi: 10.1016/j.ijmultiphaseflow.2018.03.003.

Zahoor, R., Belšak, G., Bajt, S. and Šarler, B. (2018b), "Simulation of liquid micro-jet in free expanding high-speed co-flowing gas streams", *Microfluidics and Nanofluidics*, Vol. 22 No. 8, p. 87, doi: 10.1007/s10404-018-2110-0.

Zahoor, R., Regvar, R., Bajt, S. and Šarler, B. (2020), "A numerical study on the influence of liquid properties on gas-focused micro-jets", *Progress in Computational Fluid Dynamics, an International Journal*, Vol. 20 No. 2, pp. 71-83, doi: 10.1504/PCFD.2020.106407.

Zahoor, R., Knoška, J., Bajt, S. and Šarler, B. (2021), "Experimental and numerical investigation of gas-focused liquid Micro-Jet velocity", *International Journal of Multiphase Flow*, Vol. 135, p. 103530, doi: 10.1016/j.ijmultiphaseflow.2020.103530.

Zahoor, R., Knoska, J., Gregorc, J., Bajt, S. and Sarler, B. (2019), "Validation of a computational model for a coupled liquid and gas flow in Micro-Nozzles", VIII International Conference on Computational Methods for Coupled Problems in Science and Engineering, 3 Jun 2019 - 5 Jun 2019, *Barcellona (Spain)*, p. 7, doi: 10.3204/PUBDB-2019-01908.

Zeng, W. and Fu, H. (2020), "Precise monodisperse droplet production in a flow-focusing microdroplet generator", *Chemical Engineering Research and Design*, Vol. 160, pp. 321-325, doi: 10.1016/j.cherd.2020.06.002.

Zhao, J., Ning, Z. and Lü, M. (2019a), "Large eddy simulation of Two-Phase flow pattern and transformation characteristics of flow mixing nozzle", *Journal of Mechanics*, Vol. 35 No. 5, pp. 693-704, doi: 10.1017/jmech.2018.51.

Zhao, J., Ning, Z. and Lv, M. (2020), "Experimental and numerical simulation of flow pattern evolution in a flow mixing nozzle under a moderate inlet flow rate", *ACS Omega*, Vol. 5 No. 35, pp. 22335-22347, doi: 10.1021/acsomega.0c02702.

Zhao, J., Ning, Z., Lü, M. and Wang, G. (2019b), "Numerical simulation of flow focusing pattern and morphological changes in two-phase flow inside nozzle", *Chinese Journal of Chemical Engineering*, Vol. 27 No. 1, pp. 63-71, doi: 10.1016/j.cjche.2018.08.022.

Corresponding author
Božidar Šarler can be contacted at: bozidar.sarler@fs.uni-lj.si